

Global Increases in Lethal Compound Heat Stress- Hydrological Drought Hazards under Climate Change

Jiabo Yin^{1*}, Louise Slater², Lei Gu³, Zhen Liao¹, Shenglian Guo¹, Pierre Gentine^{4,5}

¹State Key Laboratory of Water Resources and Hydropower Engineering Science, Wuhan University, Wuhan, China

²School of Geography and the Environment, University of Oxford, Oxford, UK

³School of Civil and Hydraulic Engineering, Huazhong University of Science and Technology, Wuhan, China

⁴Department of Earth and Environmental Engineering, Columbia University, New York, NY, USA

⁵Earth Institute, Columbia University, New York, NY, USA

Contents of this file

Text S1 to S3

Figures S1 to S15

Text S1. Global gauge streamflow data and quality control

We collected daily streamflow records from 1950 to 2021 at outlets of 22538 catchments, which cover diverse climatic patterns and underlying surface conditions across the globe. These data are sourced from a combination of global and national streamflow archives: (1) the Global Runoff Data Centre (GRDC); (2) the U.S. Geological Survey (USGS) National Water Information System; (3) the Australian Bureau of Meteorology; (4) the UK Centre for Ecology and Hydrology (UKCEH); (5) the Environment and Climate Change Canada (ECCC) through the Water Survey of Canada (WSC); (6) the Brazilian National Water Agency (ANA); and (7) the Ministry of Water Resources of China (MWRC); (8) the watershed management agencies affiliated with the MWRC; (9) the National Hydrological Information Centre of China; (10) Guangdong Provincial Bureau of Beijing River Administration, China; and (11) Chaohu Lake Research Institute, China.

First, we omit those stations with changing measurement instrument or station datum to keep data consistency. Second, we screen those 13958 stations with at least 20 valid years of data (with >90% completeness for each year). Thirdly, we exclude catchments with poor performance in hydrological simulation defined as a Kling-Gupta efficiency metric smaller than 0.5 in all five candidate hydrological models. Overall, these filtering steps leave 11637 catchments. Most of our selected catchments have been calibrated in Gu et al. (2022), but in this study more stations have been added in China and the streamflow series have been updated from 2018 to 2021.

Text S2. Bivariate analysis methods

The joint return period (JRP) is given as:

$$JRP = \frac{E}{1 - F_{HW} - F_{DR} + C(F_{HW}, F_{DR})} \quad (1)$$

where F_{HW} (F_{DR}) is the marginal cumulative distribution of HW_s (DR_s), and $C(F_{HW}, F_{DR})$ represents the joint distribution of F_{HW} and F_{DR} ; while E denotes the average inter-arrival time between compound events.

As there can be numerous combinations of HW_s and DR_s located on the isoline of a given JRP, the likelihood of each event must be taken into consideration. In this study, the most likely

realization is optimized by achieving the maximum joint probability density (Salvadori et al., 2016; Yin et al., 2022):

$$\begin{cases} (HW_s^*, DR_s^*) = \arg \max f(HW, DR) = c(F_{HW}, F_{DR}) \cdot f_{HW} \cdot f_{DR} \\ c[F_{HW}, F_{DR}] = \frac{dC[F_{HW}, F_{DR}]}{d(F_{HW})d(F_{DR})} \end{cases} \quad (2)$$

where $c(F_{HW}, F_{DR})$ is the copula probability density function linked to the marginal distributions; f_{HW} and f_{DR} denote the probability density functions of F_{HW} and F_{DR} , respectively; and (HW_s^*, DR_s^*) is the most likely realization under the given historical JRP.

We first construct the copula functions and derive the (HW_s^*, DR_s^*) under a given JRP during the historical period, and then calculate the updated JRP by substituting the historical (HW_s^*, DR_s^*) in the copula functions for the future period. If the future JRP decreases, it implies that the CHD risk is projected to intensify; and vice versa.

To project future changes in the joint return period (JRP) of compound heat-drought events (CHD), we implemented 75 scenarios using an impact modelling chain, which consists of three shared socioeconomic pathways (SSPs), five global climate models (GCMs) and five hydrological models (HMs) under ISIMIP3b. In this study, the overall uncertainty is estimated from the variance of the updated JRP of the historical 50-year CHD during the future period, and then it is decomposed into the uncertainty contribution of different sources and their interactions using the multivariate analysis of variance (ANOVA) method (Addor et al., 2014). The change in the climatic indicator $\Delta y_{i,j,k}$ (i.e., updated JRP of the historical 50-year CHD in this study) is assumed to follow the following model:

$$\Delta y_{i,j,k} = \mu + R_i + G_j + H_k + I_{i,j,k} \quad (3)$$

where μ represents the mean change of the model ensemble of the climatic indicator; R_i , G_j and H_k represent the effects on the climatic indicator of the i^{th} SSP, j^{th} GCM, and k^{th} HM, respectively; and $I_{i,j,k}$ represents the sum of the effects due to the interaction between different sources.

Based on the multivariate ANOVA method, the total variance (overall uncertainty, VT) can be decomposed into contributions from different sources as follows:

$$VT = VR + VG + VH + VI_{RG} + VI_{RH} + VI_{RGH} \quad (4)$$

where VR , VG , VH present the variance contributed by the effects of SSPs, GCMs and HMs, respectively; VI_{RG} , VI_{RH} and VI_{RGH} represent the variance from interaction effects between SSP-GCM, SSP-HM and SSP-GCM-HM, respectively. The fractional contributions of different sources to the overall uncertainty are obtained by dividing the variance from each source by the total variance.

Text S3. Experiments to disentangle the relative contributions of three drivers to changes in CHD hazards

We carry out three experiments to disentangle the relative contributions of three drivers to changes in CHD hazards: (a) fixing the marginal distributions of heatwave and the dependence between droughts and heatwaves in the historical period and exchanging the marginal distributions of droughts in the future period; (b) as experiment (a), but exchanging the marginal distributions of heatwaves in the future period; and (c) fixing both marginal distributions of droughts and heatwaves in the historical period and using the fitted copula for the future period.

References From the Supporting Information

- Addor, N., Rössler, O., Köplin, N., Huss, M., Weingartner, R., & Seibert, J. (2014). Robust changes and sources of uncertainty in the projected hydrological regimes of Swiss catchments. *Water Resources Research*, 50(10), 7541–7562.
- Salvadori, G., Durante, F., Michele, C. D., Bernardi, M., & Petrella, L. (2016). A multivariate copula-based framework for dealing with hazard scenarios and failure Probabilities. *Water Resources Research*, 52(5), 3701–3721.
- Yin, J., Guo, S., Wang, J. et al. (2022). Projection of droughts and their socioeconomic exposures based on terrestrial water storage anomaly over China. *Science China Earth Sciences*, 65, <https://doi.org/10.1007/s11430-021-9927-x>
- Gu, L., Chen, J., Yin, J., Slater, L. J., Wang, H. M., Guo, Q., Feng, M., Qin, H., & Zhao, T. (2022). Global increases in compound flood-hot extreme hazards under climate warming. *Geophysical Research Letters*, 49(8), e2022GL097726.

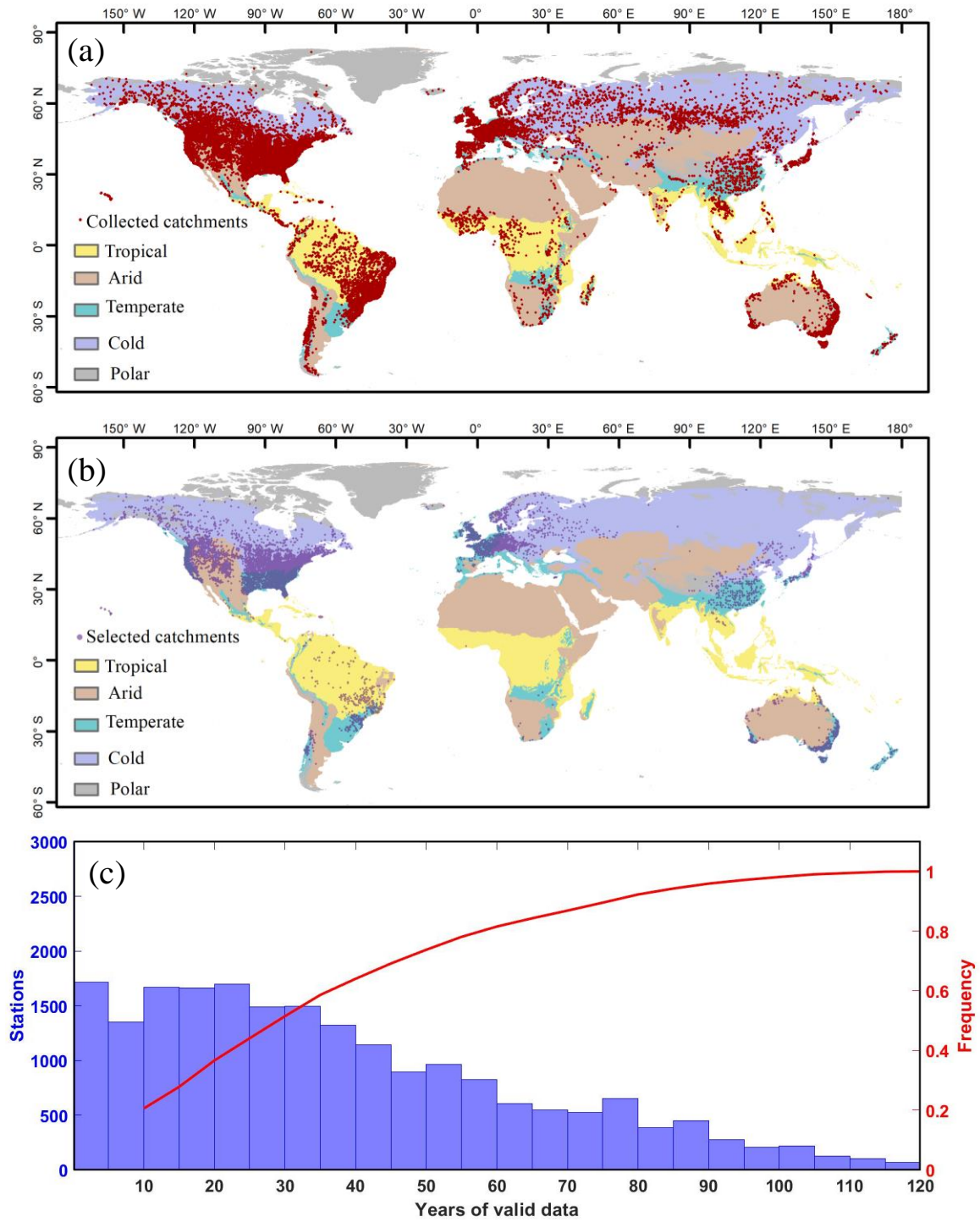


Figure S1. Global maps showing the 22538 catchments across five (tropical, arid, temperate, cold, polar) climate zones. a, All the collected catchments. b, Selected catchments. c, Histogram of years of valid data (>90% completeness for each year) for global stations.

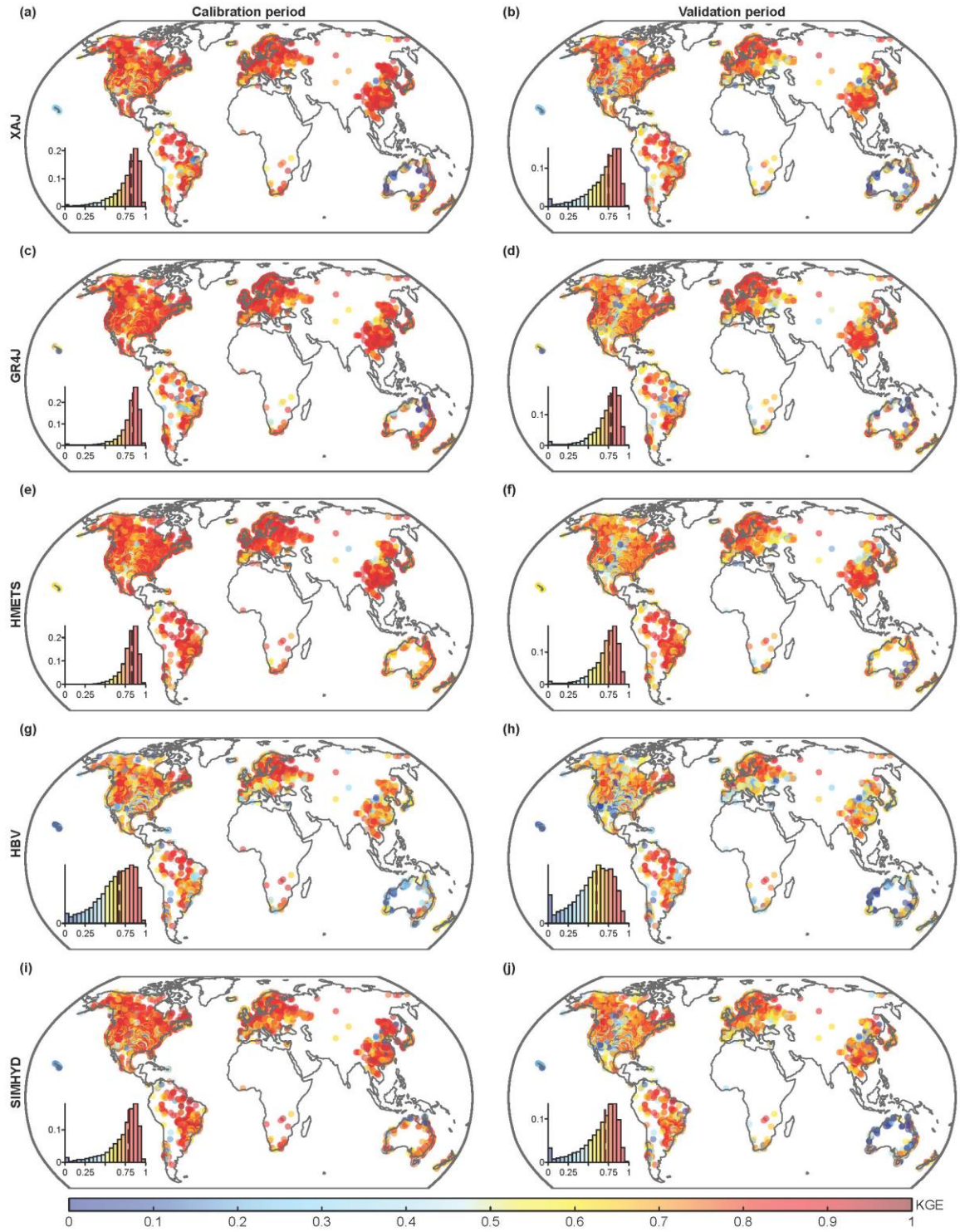


Figure S2. The KGE values of five hydrological models during calibration and validation periods over global selected catchments. Insets show the histogram of the KGE values, with the dashed vertical line representing the mean value.

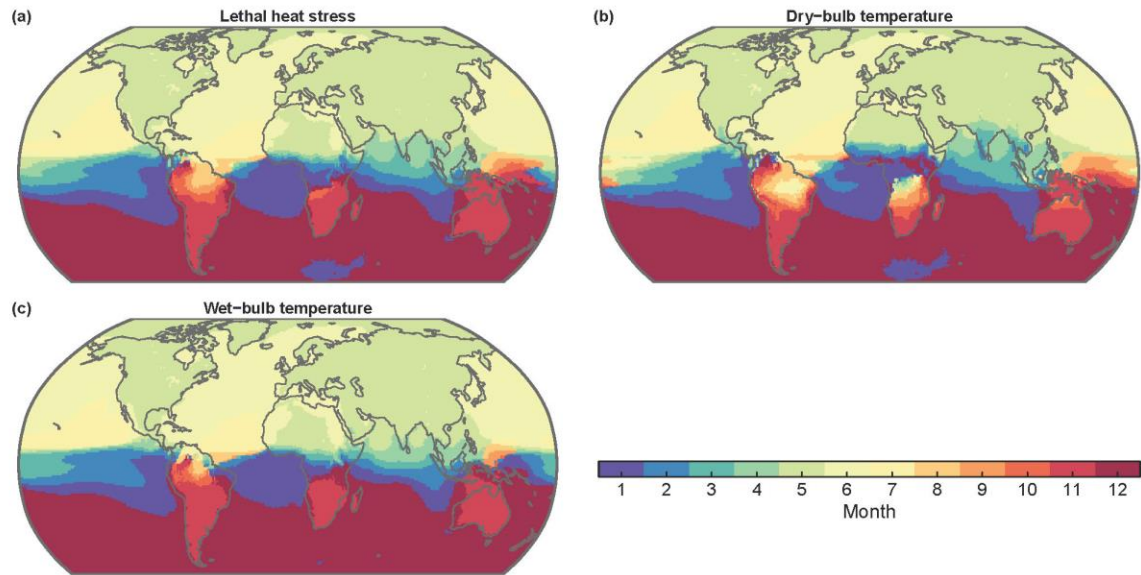


Figure S3. Warm season defined using ERA5 temperature (1979-2021). a-c, the warm season is derived by using data of lethal heat stress (a), dry-bulb temperature (b), and wet-bulb temperature (c). The starting month of the five-month period with highest mean temperature (warm season) is shown in each grid cell.

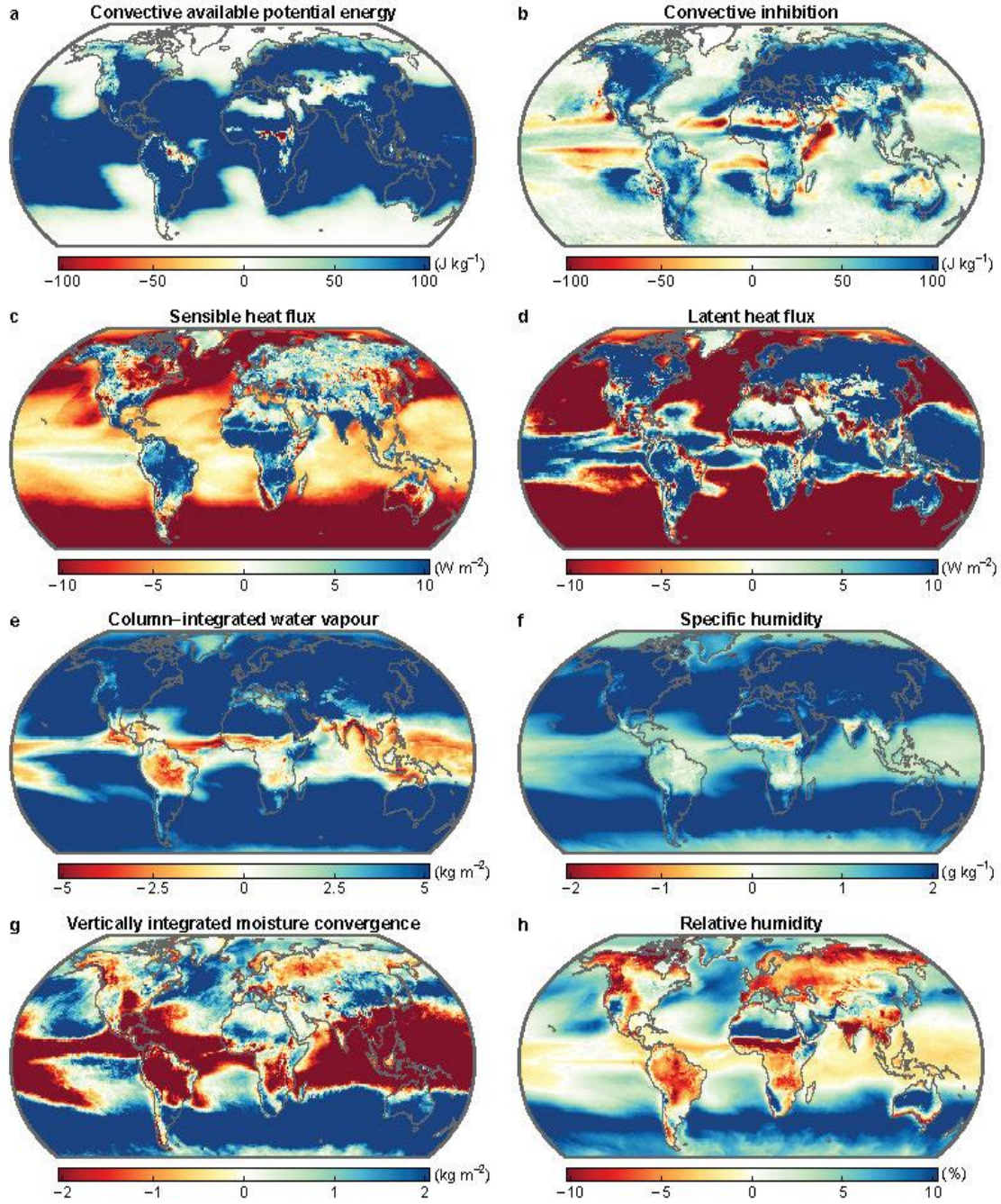


Figure S4. Anomalies of composite water and heat variables during lethal heat stress extremes. a-h, Anomalies of CAPE (a), convective inhibition (b), sensible heat flux (c), latent heat flux (d), column-integrated water vapor (e), specific humidity (f), Vertically integrated moisture convergence (g) and relative humidity (h) during extreme heat events. Anomalies of the variables are calculated as the difference between the daily values during heat stress extremes (above the 90th percentile daily T_s) and the mean daily values in the warm season in each grid cell.

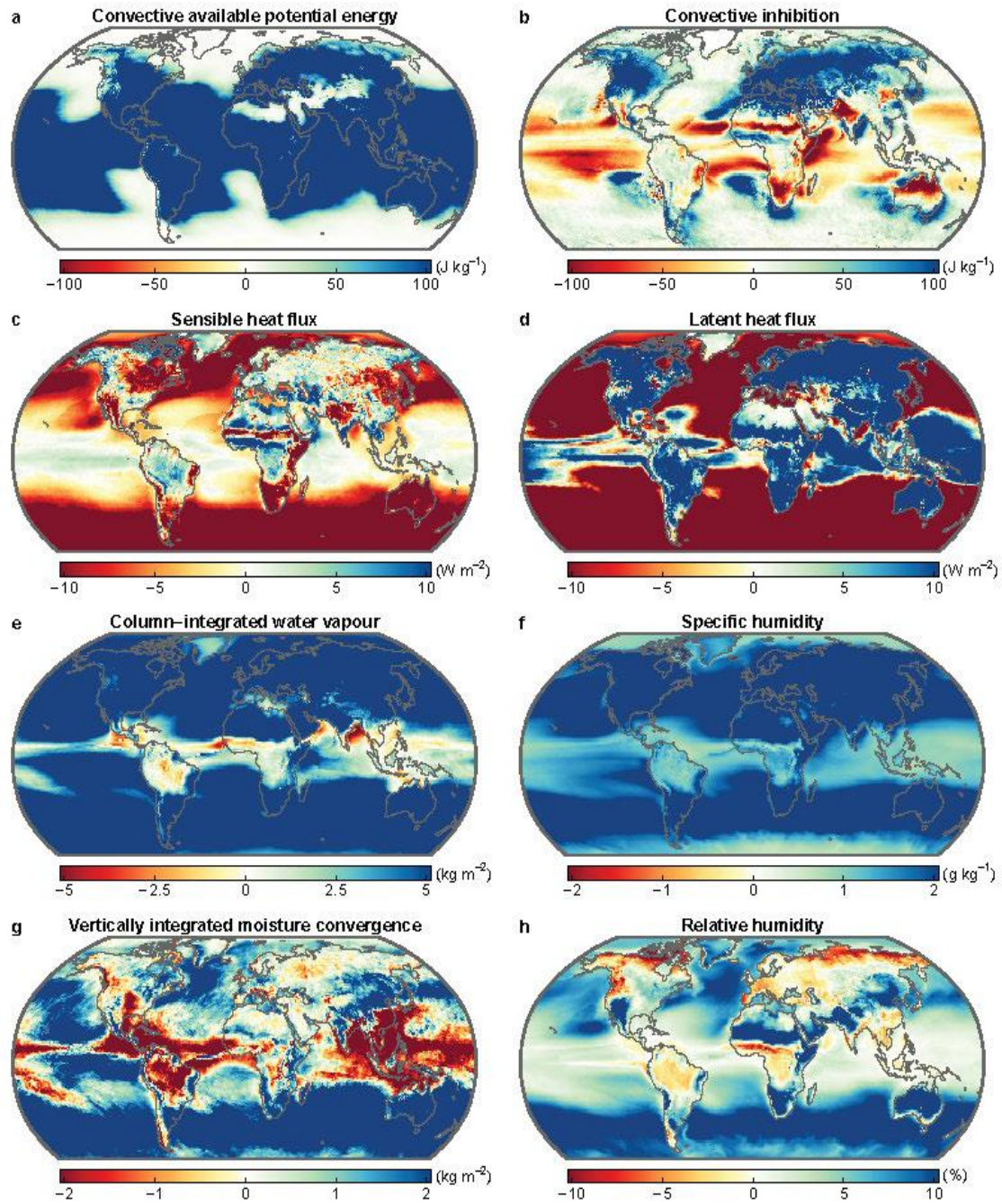


Figure S5. The same as Figure S4, but the heat stress is identified by using T_w .

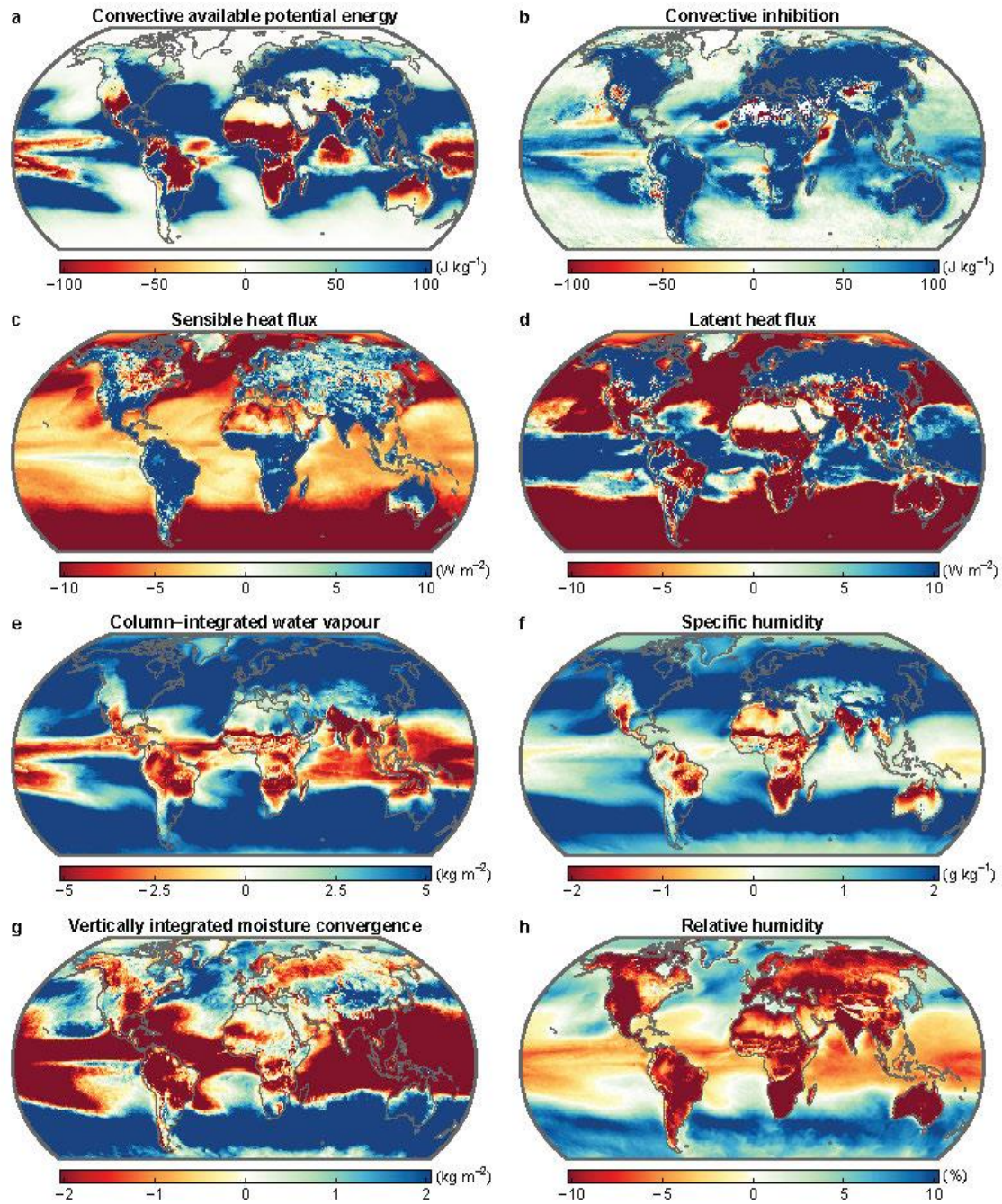


Figure S6. The same as Figure S4, but the heat stress is identified by using T_{dry} .

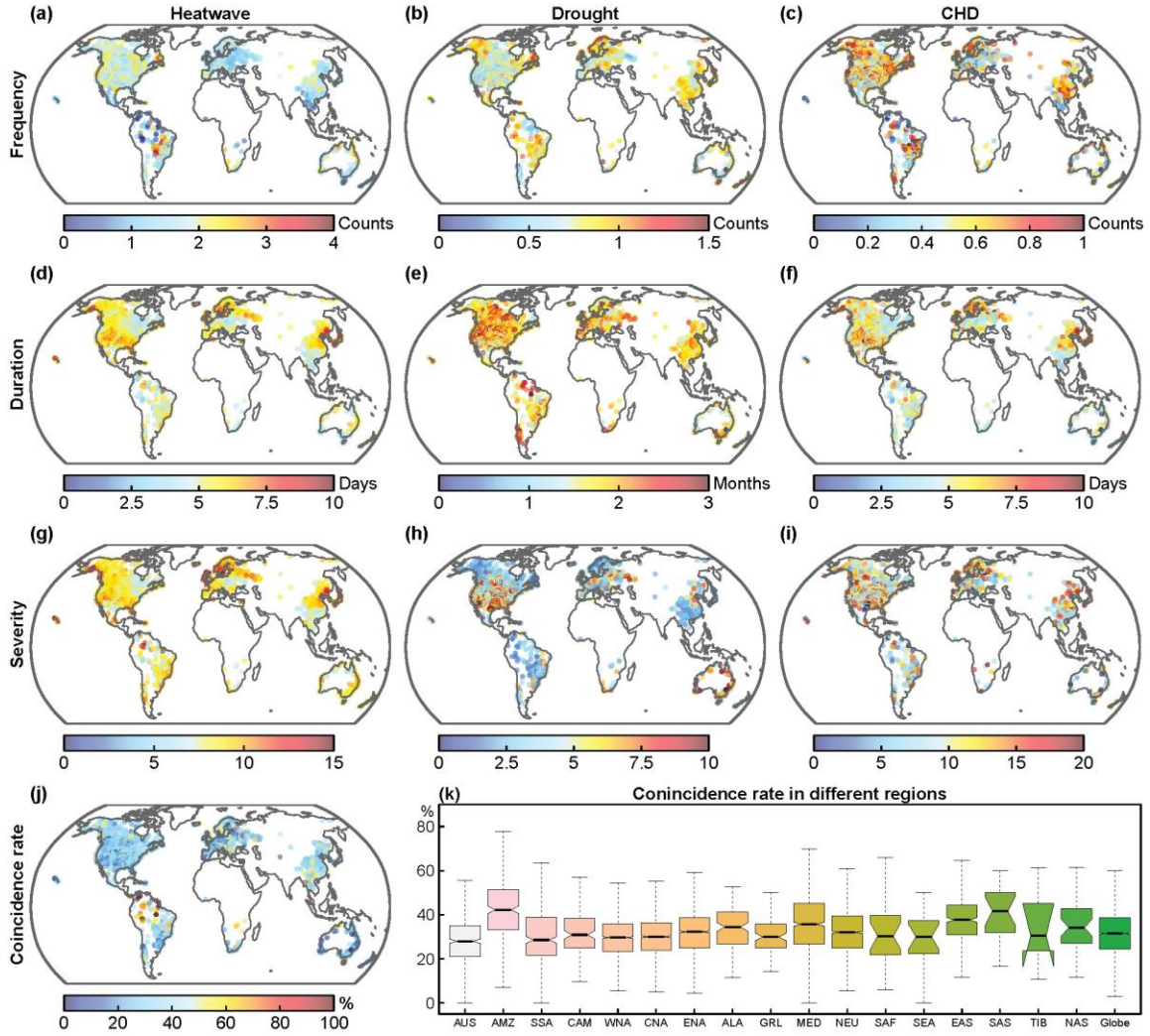


Figure S7. Global characteristics of heatwave, droughts, and CHD during 1979-2021. a-i, frequency (a-c), duration (d-f) and severity (g-i) of heatwave, droughts, and CHD. The frequency represents the total occurrence of events, while the duration and severity are averaged across all events. j-k, Global and regional distributions of the coincidence rate of CHD. Heatwaves are identified by using T_h .

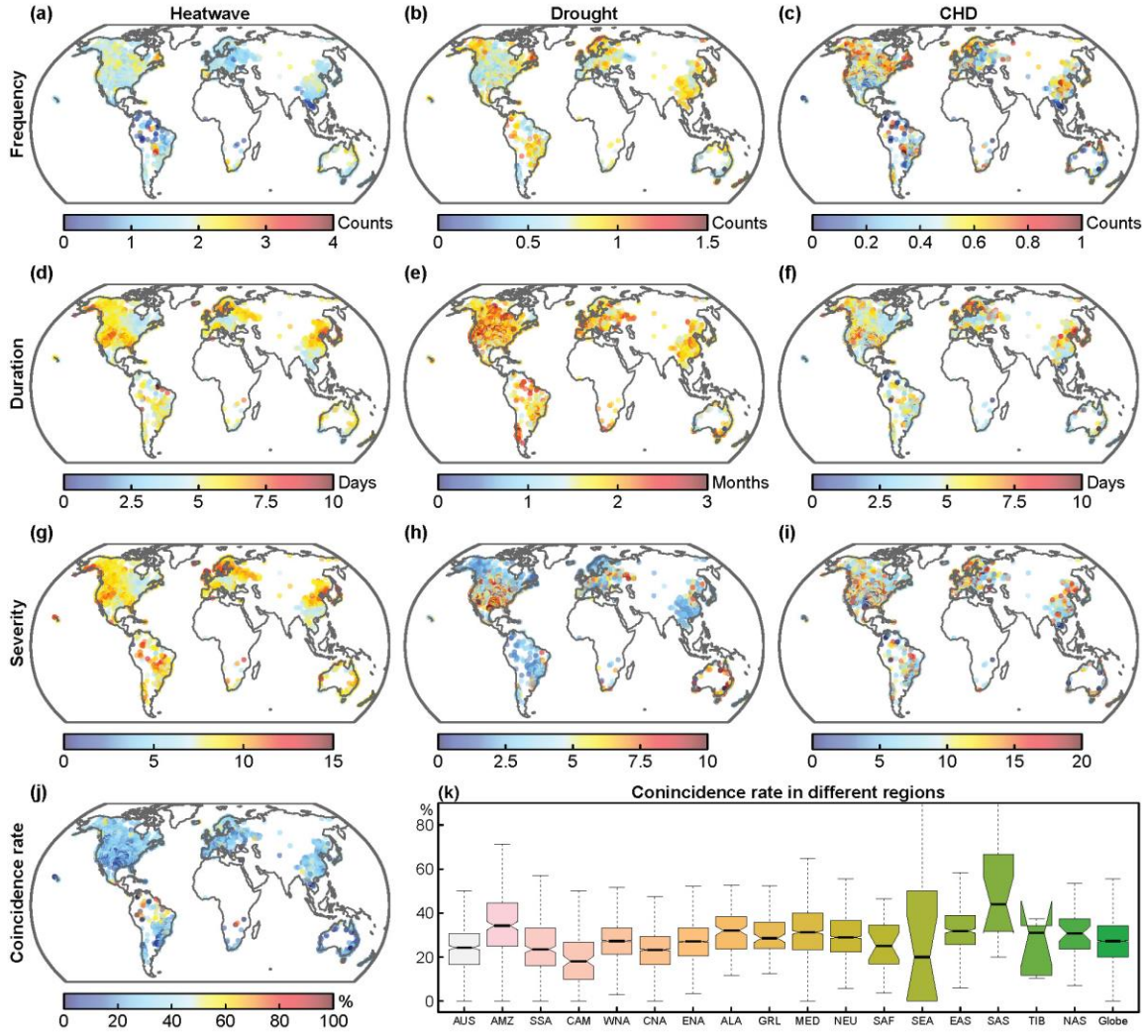


Figure S8. The same as Figure S7, but the heatwave is identified by using T_w .

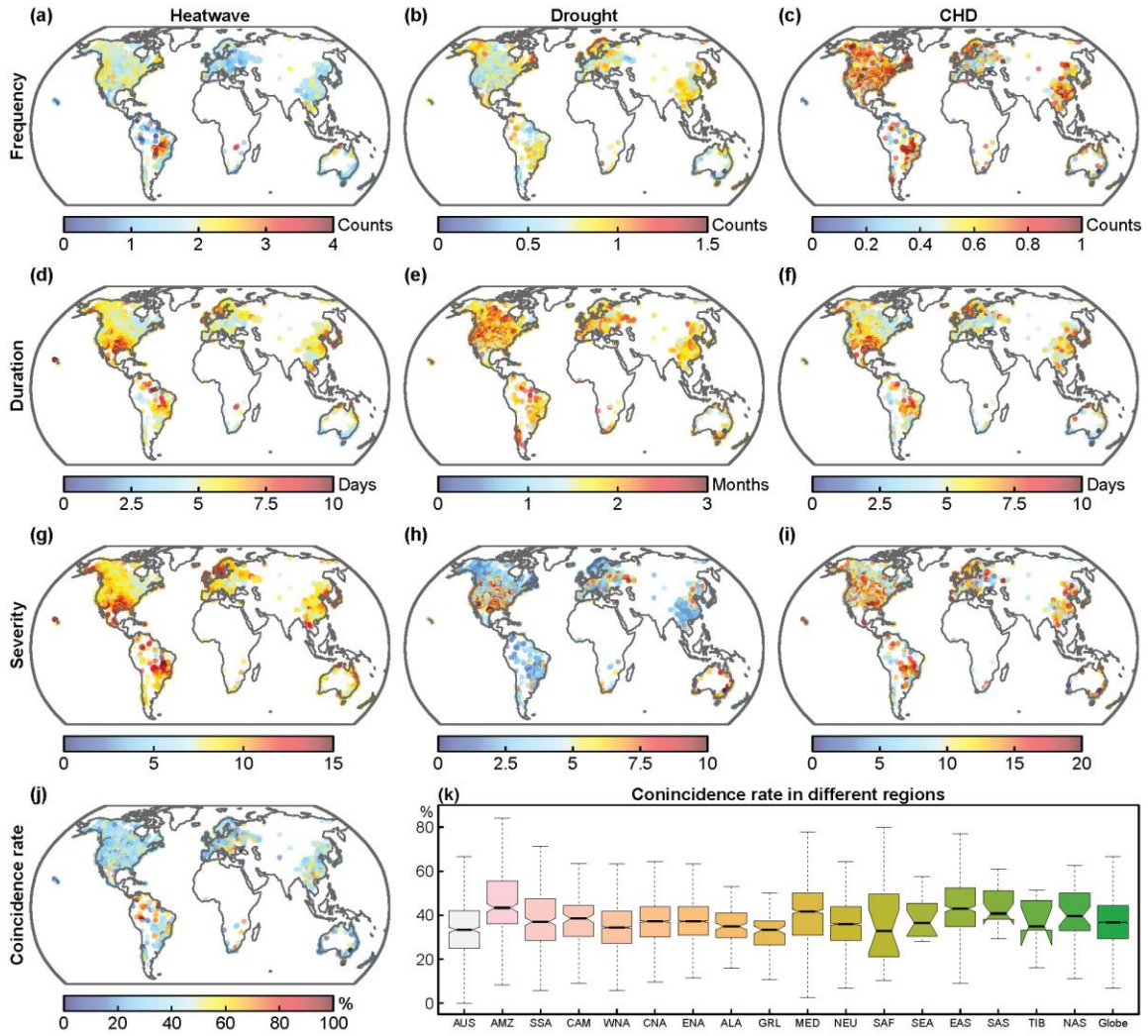


Figure S9. The same as Figure S7, but the heatwave is identified by using T_{dry} .

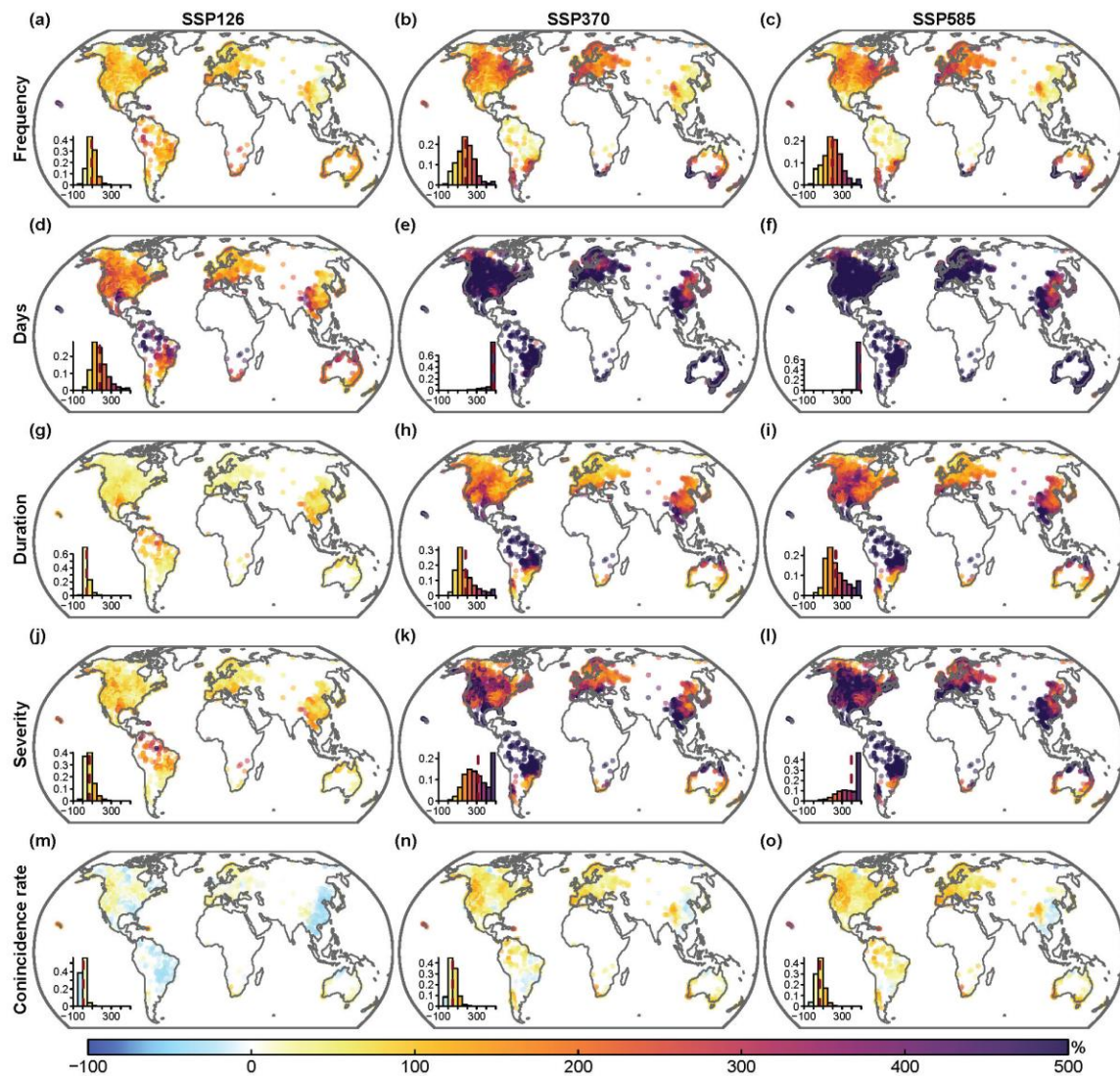


Figure S10. Future changes in the characteristics of CHD by 2071-2100 under different SSPs. Insets show the histogram of the changes, with the dashed vertical line representing the mean value.

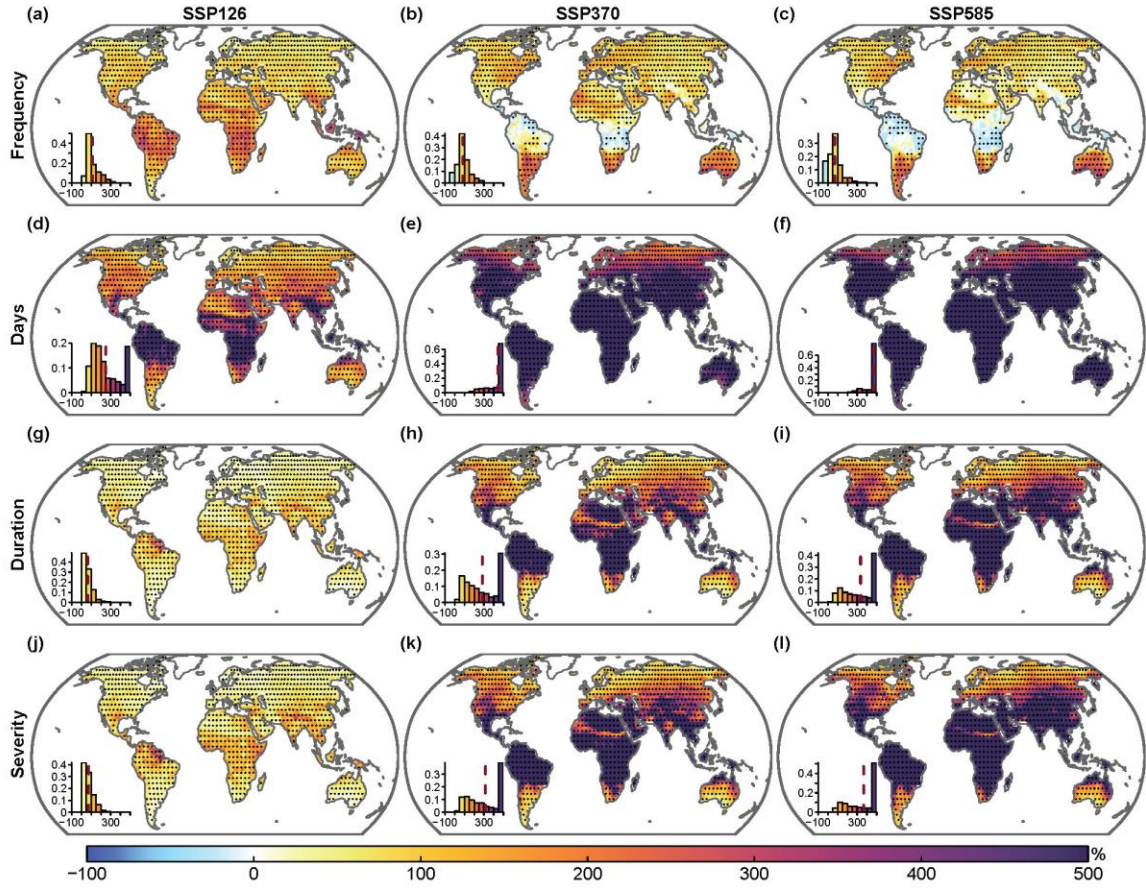


Figure S11. Future changes in the characteristics of heatwaves by 2071-2100 under different SSPs. Insets show the histogram of the changes, with the dashed vertical line representing the mean value.

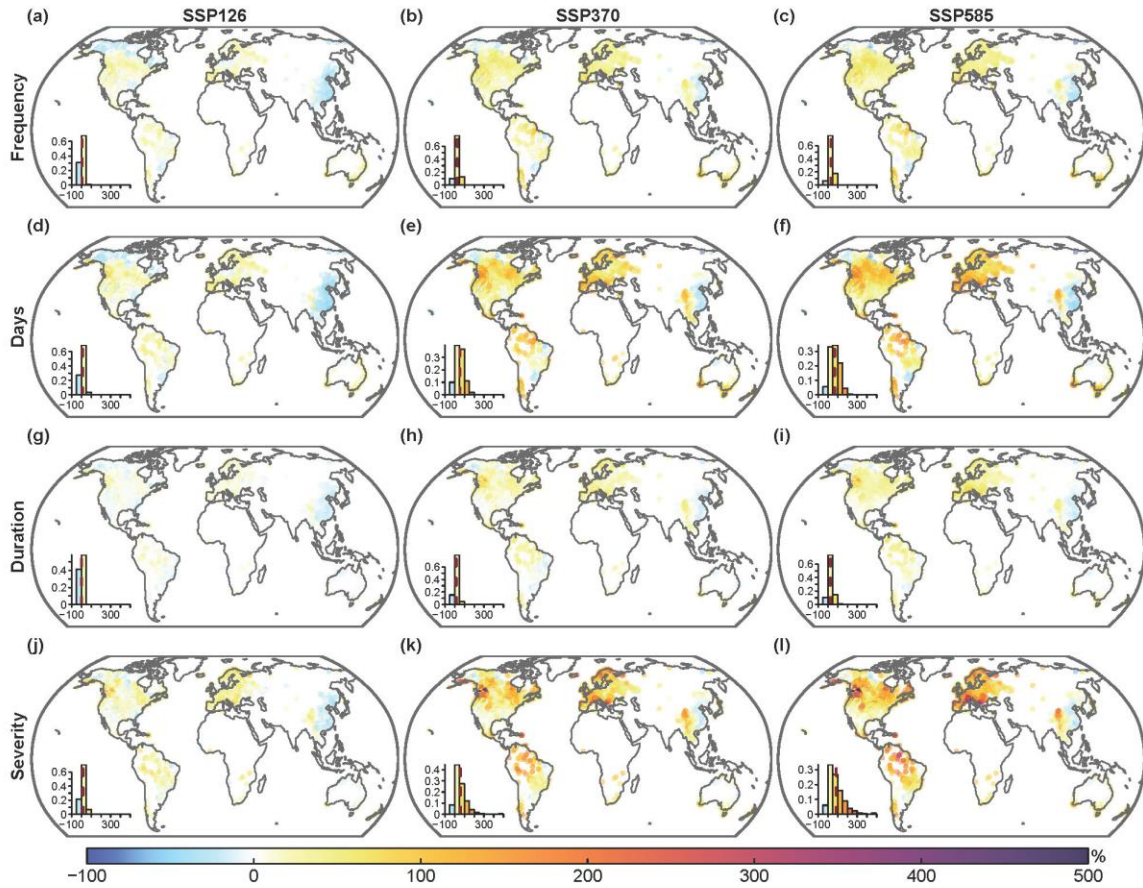


Figure S12. Future changes in the characteristics of droughts by 2071-2100 under different SSPs. Insets show the histogram of the changes, with the dashed vertical line representing the mean value.

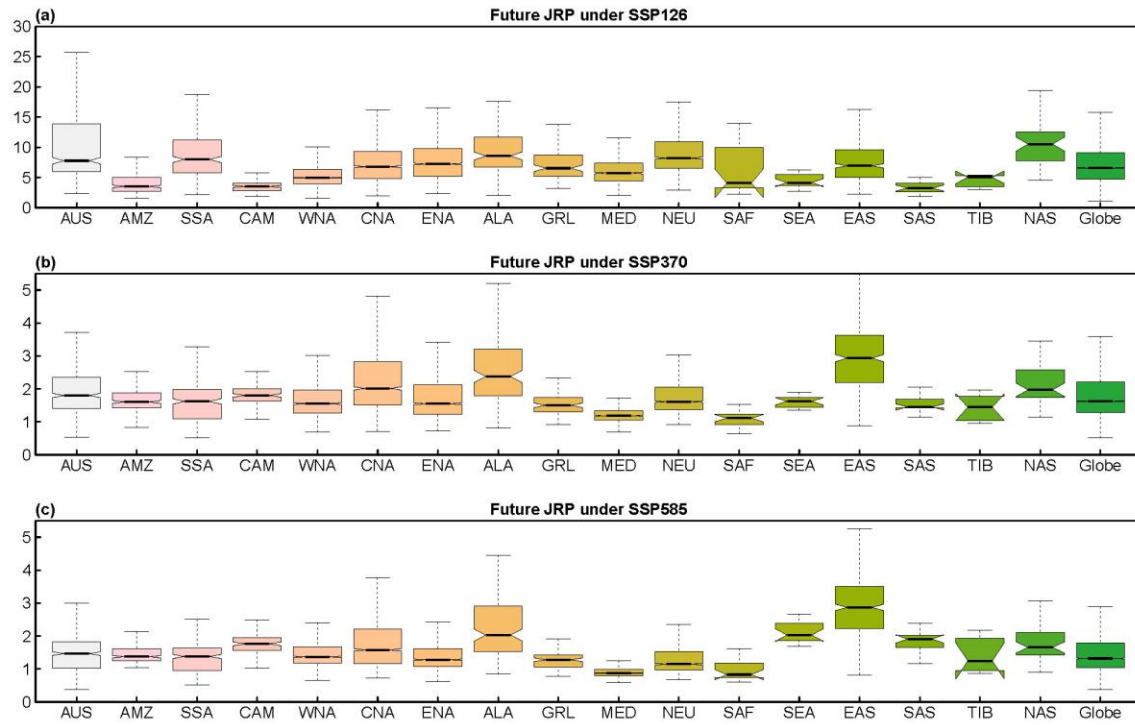


Figure S13. Future joint return period of the historical 50-year CHD in different regions.

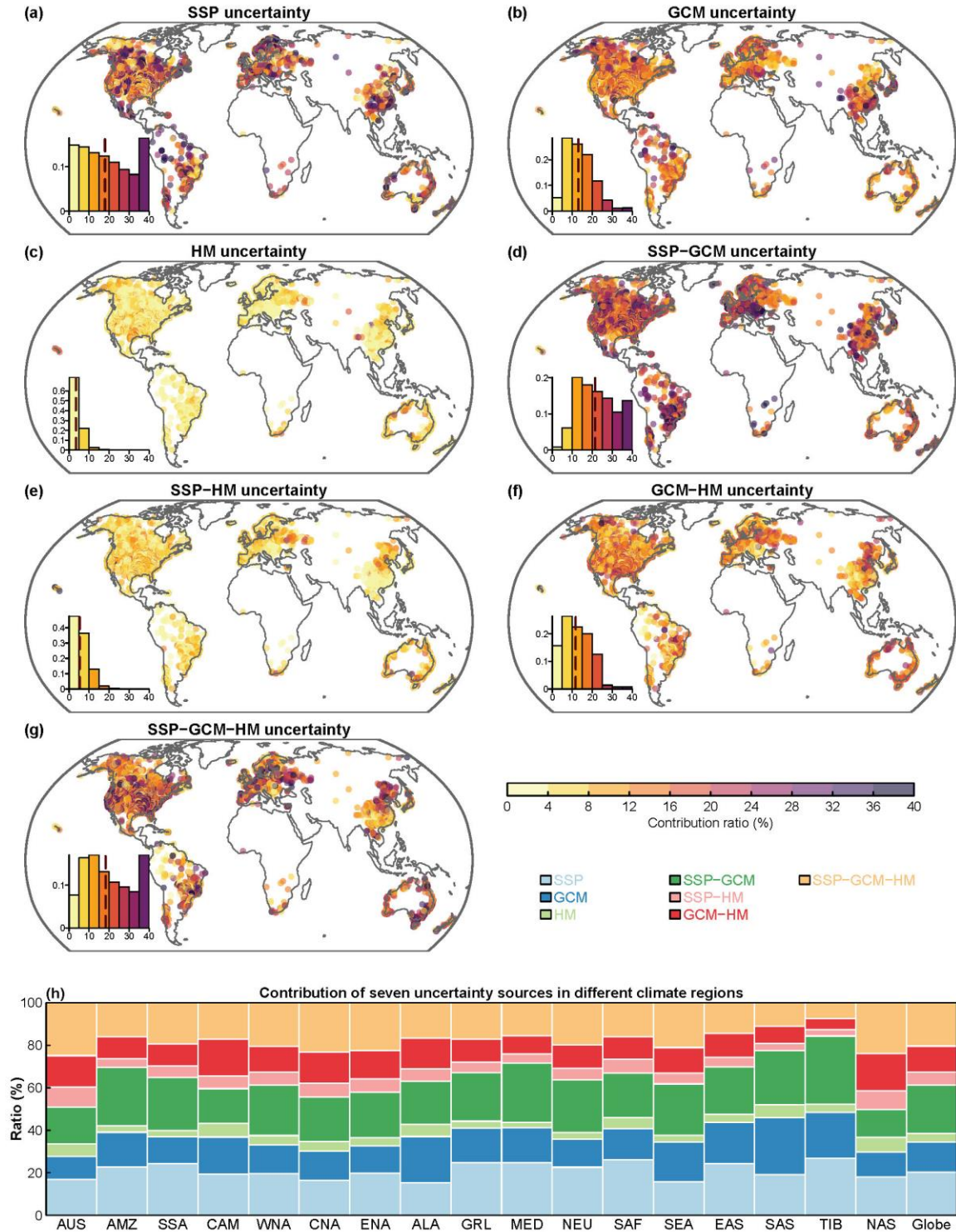


Figure S14. Contribution ratios of estimation uncertainty from seven different sources. a-c, Uncertainty of estimating future JRP from different SSPs (a), GCMs (b) or HMs (c). d-g, Uncertainty from interaction of SSP and GCM (d), SSP and HM (e), GCM and HM (f) as well as SSP, GCM and HM (g). h, Average contribution ratios of seven uncertainty sources in different Giorgi climate regions and in the global landmass (Glob). Insets in a-g show the histogram of the contribution ratio, with the dashed vertical line representing the mean value.

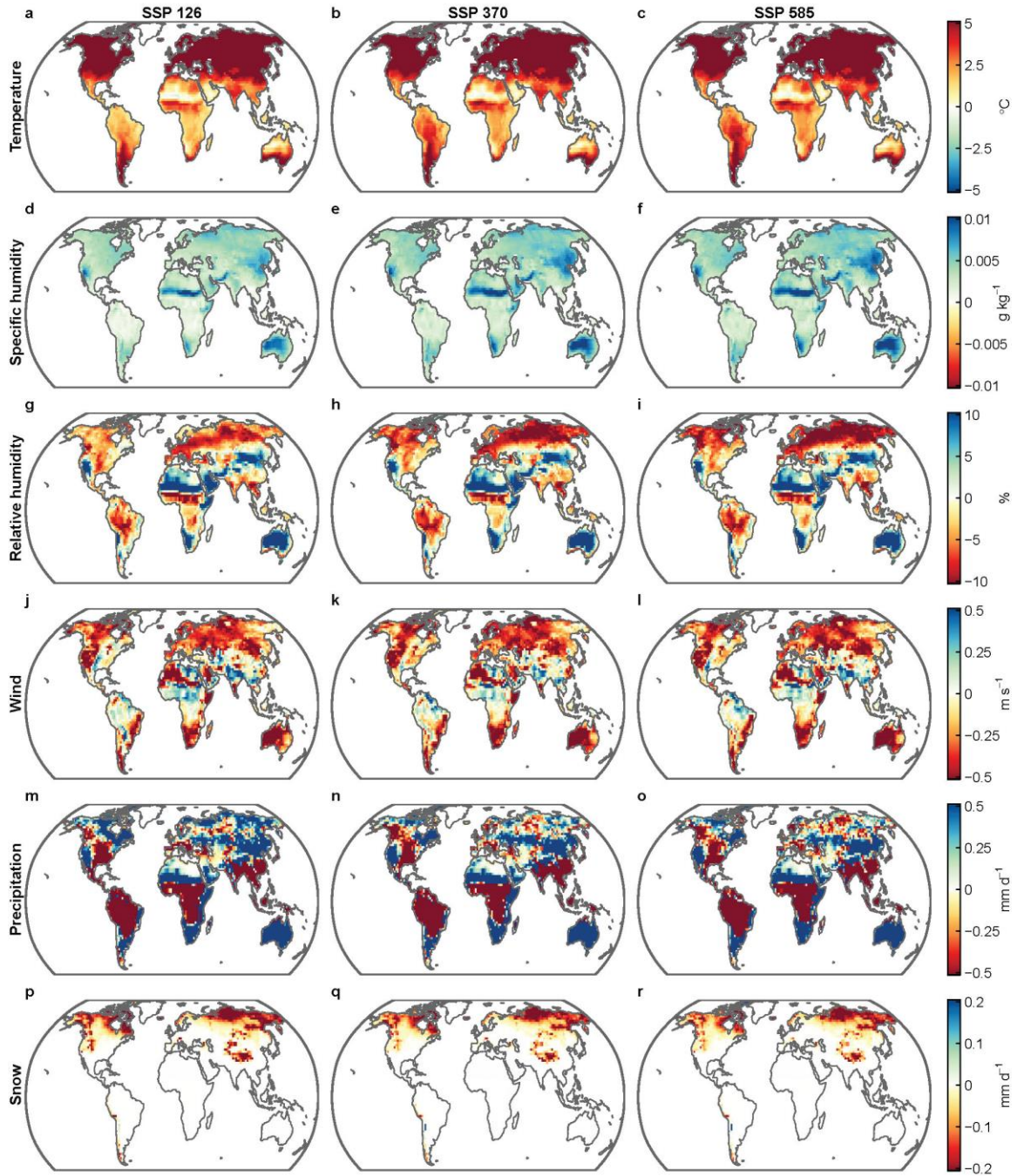


Figure S15. Anomalies of daily meteorological variables during lethal heat stress in 2071-2100. Anomalies of the variables are calculated as the difference between the daily values in heat stress extremes (above the 90th percentile of daily T_h during the future period) and the mean daily values in the warm season in each grid cell.